AIAA SciTech Forum
9 - 13 January 2017, Grapevine, Texas
55th AIAA Aerospace Sciences Meeting

CrossMark
click for updates

Stall Flutter Simulation of a Transonic Axial Compressor Stage Using a Fully Coupled Fluid-Structure Interaction

Jiaye Gan[*] Hong-Sik Im [†] Gecheng Zha[‡]
Dept. of Mechanical and Aerospace Engineering
University of Miami
Coral Gables, FL 33124
gzha@miami.edu

Downloaded by Gecheng Zha on March 3, 2017 | http://arc.aiaa.org | DOI: 10.2514/6.2017-0783

Abstract

In this paper, numerical simulation of stall flutter for full annulus NASA Stage 35 is conducted using a fully coupled fluid/structure interaction. Time accurate compressible 3D Navier-Stokes equations with Spalart-Allmaras turbulence model are solved with a system of 5 decoupled structural modal equations in a fully coupled manner. The 3rd order WENO scheme for the inviscid flux and 2nd order central difference for the viscous terms are used to accurately capture the interactions of the fluid and structure. Delayed detached eddy simulation is also applied to predict the flow induced vibration at near and stall conditions for comparison. The mechanism and aerodynamic damping behavior causing the stall flutter are analyzed. The effect of rotor stator interaction on the onset of flutter is studied. The fully coupled FSI simulation shows that Stage 35 has stall flutter at rotating stall.

1 Introduction

Stall flutter is an aeromechanic instability that usually occurs at part-speed operation in turbomachinery. It occurs when the energy absorbed by the blades from surrounding fluid exceeds the dissipating energy of the material and mechanical damping. The blade will vibrate exponentially and cause possible structure failure. Stall flutter could occur subsonic, transonic and supersonic incoming flow conditions. Transonic blades are widely used in modern fans/compressor, and are often prone to transonic stall flutter at off-design conditions. The flutter problem becomes more and more challenging with the modern light structures of compressor/fan such as blisk or integrated blade disks, which have little mechanical damping.

Transonic flutter near stall conditions in turbomachinery are highly unsteady, non-linear and three dimensional, which include flow induced vibration, flow separation, shock unsteadiness, shock wave/turbulent boundary interactions. The driving mechanism of the stall flutter in transonic turbomachinery may varied between the large separation and shock wave oscillation. Lepicovsky et al.[1] shows that the transonic stall flutter is triggered by the high frequency stall cell propagation in separated area on the airfoil suction side. There are no shock waves at high subsonic inlet Mach numbers (about 0.95) when transonic stall flutter occurred in their study[1]. Shwa et al.[2] demonstrates that the energy from shock wave oscillations is not strong enough to induce the transonic stall flutter based on a shock wave motion model. On the other hand, unsteady shock oscillation rather than blade stall was found to be the driving mechanism for flutter instability in a transonic fan[3]. The shock location and movement and its relation

[*] Ph.D.
[†] Ph.D., Currently an engineer at Honeywell
[‡] Ph.D., Professor, Director of Aerodynamics and CFD Lab

Copyright © 2017 by the American Institute of Aeronautics and Astronautics, Inc. All rights reserved.

to the inter blade phase angle contributes significantly to the variation in the aerodynamic damping[4]. The comparison with measured data for the onset of a transonic fan flutter by Chew et al.[5] shows that the shock movement of the blade passage appears to be an important parameter causing the fan flutter due to the interaction of the passage shocks with the suction surface boundary layer. Vahdati et al.[6] shows that the flow separation behind the shock on the suction surface is the key driver of a wide-chord transonic fan flutter. Another study shows that shock has both stabilizing and destabilizing effect with the inter-blade phase angle and location of shock having a significant impact on stability[7, 8]. All these studies indicate the complexity of the stall flutter that can be induced by different flow phenomena. Accurate simulation of compressor/fan flutter is crucial for industrial design and diagnosis.

To achieve high fidelity simulation of nonlinear fluid/structural instabilities during the fan/compressor flutter, the governing equations of structural and fluid motion should be simultaneously solved in order to capture the flow and structure responses at the same time as happening in reality. However, many of fluid-structural interaction (FSI) simulations are implemented by a loosely coupled procedure, i.e the structural response lags behind the flow solver by one or several time steps[9]. For example, Gnesin et al.[10] solved the unsteady Euler equations with the modal approach for the structure analysis in an loosely coupled manner. Doi et al.[11] loosely coupled an explicit Runge-Kutta multigrid flow solver with a FEM structure solver to predict the aeroelastic forced responses of NASA Rotor 67 blade. In the work of Carstens et al.[12] and Sayma et al.[13], the structural part of the governing equations is time-integrated using Newmark scheme, while the unsteady air loads are computed at every time step by a Navier-Stokes code in an loosely coupled manner. Chew et al.[5] used inviscid linearized model, to capture stall flutter (or referred to as part-speed flutter) of a civil wide chord fan and a low aspect ratio military fan engine. Due to neglecting viscous terms, end wall boundary layers and tip clearance, their computation fails to show any signs of flutter instability, which was observed in the testing. It is also shown that the conventional energy method, in which the blade vibration and aerodynamic forces may be treated independently, could not accurately capture the modern fan flutter boundary whereas the coupled mode flutter analysis methods do[14].

In the work of Im et al.[8], a fully coupled FSI developed by Chen et al.[15] is extended for turbomachinery by implementing an advanced blade tip deforming mesh technique to capture the transonic rotor flutter. In the fully coupled FSI[15], the governing equations of structural and fluid motion are simultaneously solved by exchanging the unsteady aerodynamic force and structural displacement within each physical time step via a successive iteration on the pseudo-time step. The fully coupled FSI methodology adopted in this study is shown to accurately predict the flutter boundary of a transonic single rotor[8] and AGARD wing with the shock/boundary layer interaction[16, 17].

The purpose of this paper is to simulate a transonic stall flutter in a full stage with rotor-stator interaction and traveling wave. The full annulus of NASA Stage 35 is selected to demonstrate this capability. Simulating the flutter mechanism in a full stage environment is more realistic than the previous simulation of single rotor blade row. It is an important tool to improve the industrial aeromechanic design and analysis with more reliable design.

2 Aerodynamic Model

An accurate Riemann solver is necessary to capture the shock wave turbulent boundary layer interaction in aeroelastic analysis. The Low Diffusion E-CUSP (LDE) Scheme[18] is used to evaluate the inviscid fluxes. The LDE scheme can capture crisp shock profile and exact contact surface discontinuities as accurately as the Roe scheme[18]. However, it is simpler and more CPU efficient than the Roe scheme due to no matrix operation. The 3rd order WENO scheme for the inviscid flues and 2nd order central differencing scheme for viscous terms[19] are used. An implicit unfactored Gauss-Seidel line iteration is used to achieve high convergence rate. The high-scalability parallel computing is applied to

Downloaded by Gecheng Zha on March 3, 2017 | http://arc.aiaa.org | DOI: 10.2514/6.2017-0783

save wall clock time[20]. The Spalart-Allmaras one equation turbulence model is employed.

2.1 Governing Equations

The equation of motion of fluid flow for turbomachinery in a relative frame of reference can be derived by adding the effects of Coriolis force ($2\Omega\times\mathbf{V}$) and the centrifugal force($\Omega\times\Omega\times\mathbf{r}$) to the equation for the absolute frame. Expanding this momentum equation with continuity and energy equations in a rotating Cartesian system(x, y, z) as shown in Fig. 1 and applying coordinate transformation to the generalized coordinate system(ξ, η, ζ), the dimensionless spatially filtered 3D Navier-Stokes equations can be expressed as the following conservative form:

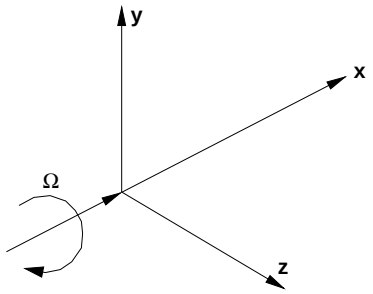

Figure 1: The Cartesian system with y and z axes rotation about the x-axis at a constant speed Ω

$$\frac{\partial \mathbf{Q}}{\partial t}+\frac{\partial \mathbf{E}}{\partial \xi}+\frac{\partial \mathbf{F}}{\partial \eta}+\frac{\partial \mathbf{G}}{\partial \zeta}=\frac{1}{Re}\left(\frac{\partial \mathbf{E}_v}{\partial \xi}+\frac{\partial \mathbf{F}_v}{\partial \eta}+\frac{\partial \mathbf{G}_v}{\partial \zeta}\right)+\mathbf{S} \tag{1}$$

The inviscid flux vector $\mathbf{E}$, the viscous flux vector $\mathbf{E_v}$ and the source term vector $\mathbf{S}$ are expressed as follows and the rest can be expressed following the symmetric rule.

$$\mathbf{E}=\begin{pmatrix} \bar{\rho}U \\ \bar{\rho}\tilde{u}U+l_x\bar{p} \\ \bar{\rho}\tilde{v}U+l_y\bar{p} \\ \bar{\rho}\tilde{w}U+l_z\bar{p} \\ \left(\bar{\rho}\tilde{e}+\bar{p}\right)U-l_t\bar{p} \\ \bar{\rho}\tilde{\nu}U \end{pmatrix} \tag{2}$$

$$\mathbf{E_v}=\begin{pmatrix} 0 \\ l_k\bar{\tau}_{xk} \\ l_k\bar{\tau}_{yk} \\ l_k\bar{\tau}_{zk} \\ l_k\left(\tilde{u}_i\bar{\tau}_{ki}-\bar{q}_k\right) \\ \frac{\bar{\rho}}{\sigma}\left(\nu+\tilde{\nu}\right)\left(\mathbf{1}\bullet\nabla\tilde{\nu}\right) \end{pmatrix} \tag{3}$$

Downloaded by Gecheng Zha on March 3, 2017 | http://arc.aiaa.org | DOI: 10.2514/6.2017-0783

$$\mathbf{S} = \frac{1}{J}\begin{pmatrix} 0 \\ 0 \\ \bar{\rho}{R_o}^2 y + 2\bar{\rho}R_o w \\ \bar{\rho}{R_o}^2 z - 2\bar{\rho}R_o v \\ 0 \\ \bar{\rho}C_{b1}\left(1-f_{t2}\right)\tilde{S}\tilde{\nu} + \\ \frac{1}{Re}\left[-\bar{\rho}\left(C_{w1}f_w - \frac{C_{b1}}{\kappa^2}f_{t2}\right)\left(\frac{\tilde{\nu}}{d}\right)^2\right. \\ \left.+\frac{\bar{\rho}}{\sigma}C_{b2}\left(\nabla\tilde{\nu}\right)^2 - \frac{1}{\sigma}\left(\nu+\tilde{\nu}\right)\nabla\tilde{\nu}\bullet\nabla\bar{\rho}\right] \\ +Re\left[\bar{\rho}f_{t1}\left(\Delta q\right)^2\right] \end{pmatrix} \tag{4}$$

where the overbar denotes the spatial filtered quantity, and the tilde is used to denote the Favre filtered quantity. U, V and W are the contravariant velocities in ξ, η, ζ directions. For an example, U is defined as follows.

$$U = l_t + \mathbf{l}\bullet\mathbf{V} = l_t + l_x\tilde{u} + l_y\tilde{v} + l_z\tilde{w} \tag{5}$$

$$l_t = \frac{\xi_t}{J}d\eta d\zeta, \quad l = \frac{\nabla\xi}{J}d\eta d\zeta \tag{6}$$

When the grid is stationary, $l_t = 0$. In the current discretization, $d\eta = d\zeta = 1$.

The shear stress $\bar{\tau}_{ik}$ and total heat flux $\bar{q}_k$ in Cartesian coordinates is given by

$$\bar{\tau}_{ik} = \left(\mu + \mu_{DES}\right)\left[\left(\frac{\partial\tilde{u}_i}{\partial x_k} + \frac{\partial\tilde{u}_k}{\partial x_i}\right) - \frac{2}{3}\delta_{ik}\frac{\partial\tilde{u}_j}{\partial x_j}\right] \tag{7}$$

$$\bar{q}_k = -\left(\frac{\mu}{Pr} + \frac{\mu_{DES}}{Pr_t}\right)\frac{\partial\tilde{T}}{\partial x_k} \tag{8}$$

where μ is determined by Sutherland's law. The above equations are in the tensor form, where the subscripts i, k represents the coordinates x, y, z and the Einstein summation convention is used. Eq.(7) and (8) are transformed to the generalized coordinate system.

The equation of state as a constitutive equation relating density to pressure and temperature in the relative frame is defined as

$$\bar{\rho}\tilde{e} = \frac{\bar{p}}{(\gamma-1)} + \frac{1}{2}\bar{\rho}(\tilde{u}^2 + \tilde{v}^2 + \tilde{w}^2) - \frac{1}{2}\bar{\rho}r^2\Omega^2 \tag{9}$$

where r $(= \sqrt{y^2+z^2})$ is the radius from the rotating axis, x in this study. For simplicity, all the bar and tilde in above equations will be dropped in the rest of this paper.The turbulence Reynolds stresses are closed by employing Spalart-Allmaras model[21, 8].

2.2 Time Marching Scheme

The 2nd order implicit method is used with the dual time stepping method[22, 19]. A pseudo temporal term $\frac{\partial Q}{\partial\tau}$ is added to the governing equation Eq. (1). This term vanishes at the end of each physical time step, and has no influence on the accuracy of the solution. The pseudo temporal term is discretized with first order Euler scheme. Let m stand for the iteration index within a physical time step, the semi-discretized governing equation can be expressed as

$$\begin{aligned}\left[\left(\tfrac{1}{\Delta\tau} + \tfrac{1.5}{\Delta t}\right)I - \left(\tfrac{\partial R}{\partial\mathbf{Q}}\right)^{n+1,m}\right]\delta\mathbf{Q^{n+1,m+1}} \\ = R^{n+1,m} - \tfrac{\mathbf{3Q^{n+1,m} - 4Q^n + Q^{n-1}}}{2\Delta t}\end{aligned} \tag{10}$$

Downloaded by Gecheng Zha on March 3, 2017 | http://arc.aiaa.org | DOI: 10.2514/6.2017-0783

where $\Delta\tau$ is the pseudo time step, and R is the net flux of the discretized Navier-Stokes equations.

3 Boundary Conditions

It is convenient for turbomachinery to express the boundary conditions in Cylindrical system. Coordinates mapping between the Cartesian (x, y, z) and Cylindrical system(x, θ, r) is given as

$$\begin{pmatrix} V_x \\ V_\theta \\ V_r \end{pmatrix} = \begin{pmatrix} u \\ v \cdot sin\theta - w \cdot cos\theta \\ v \cdot cos\theta + w \cdot sin\theta \end{pmatrix} = \begin{pmatrix} u \\ \frac{v \cdot z - w \cdot y}{r} \\ \frac{v \cdot y + w \cdot z}{r} \end{pmatrix} \tag{11}$$

where u, v, and w are the relative velocity components in the x, y, and z coordinate directions respectively. The absolute velocity components(C_x, C_θ, C_r) are related to the relative velocity components(V_x, V_θ, V_r) using the rotor wheel speed$(r\Omega)$ as

$$\begin{pmatrix} C_x \\ C_\theta \\ C_r \end{pmatrix} = \begin{pmatrix} V_x \\ V_\theta - r\Omega \\ V_r \end{pmatrix} \tag{12}$$

At the rotor inlet, the radial distributions of total pressure P_o, total temperature T_o, swirl angle α and pitch angle β are specified from the experiment[23]. The velocity is taken from the computational domain by the extrapolation in order to determine the rest of variables. First, we assume that the speed of sound a is constant at the inlet boundary. Then, the static temperature is obtained by

$$T_b = T_o[1 - \frac{\gamma - 1}{2}(\frac{C_i}{a_o})^2] \tag{13}$$

where the subscripts i represents the first interior cell and subscripts b indicates the first ghost cell of the boundary. C_i is the absolute velocity of the first interior cell and a_o is the total speed of sound defined by

$$\frac{a_o^2}{\gamma - 1} = \frac{a_i^2}{\gamma - 1} + \frac{C_i^2}{2} \tag{14}$$

Using the isentropic relations, the absolute velocity(C_b), the static pressure(p_b) and density(ρ_b) are determined by

$$|C_b| = \frac{1}{M_\infty}\sqrt{\frac{2}{\gamma - 1}(T_o - T_b)} \tag{15}$$

$$p_b = P_o\left(\frac{T_b}{T_o}\right)^{\frac{\gamma}{\gamma - 1}} \tag{16}$$

$$\rho_b = \frac{p_b \gamma}{a_b^2} \tag{17}$$

Then, the velocity components are decoupled and the conservative variables are found as the following:

$$\begin{pmatrix} \rho \\ \rho V_x \\ \rho V_r \\ \rho V_\theta \\ \rho e \end{pmatrix}_b = \begin{pmatrix} \rho_b \\ \rho_b C_m \cdot cos\beta \\ \rho_b C_m \cdot sin\beta \\ \rho_b(C_m \cdot tan\alpha - r\Omega) \\ \frac{p_b}{(\gamma - 1)} + \frac{\rho_b}{2}(V_x^2 + V_r^2 + V_\theta^2 - r^2\Omega^2) \end{pmatrix} \tag{18}$$

At the rotor outlet, the static pressure(p_b) is specified. The components of velocity(u, v, w) are extrapolated from the computational domain. The radial distributions of the static pressure from

Downloaded by Gecheng Zha on March 3, 2017 | http://arc.aiaa.org | DOI: 10.2514/6.2017-0783

the experiment[23] is used for the single passage validation. For the rotating stall simulations, the pressure at the peak of the rotor speed line is applied for the back pressure condition since axial compressors operating near the peak of their pressure rise characteristic have the potential to induce rotating stall[24, 25, 26]. Then, the radial distributions of the back pressure are determined by solving the simplified radial equilibrium equation(19) that can reflect the nonuniform variations of the static pressure across the full annulus.

$$\frac{1}{\rho}\frac{\partial p_b}{\partial r} = \frac{V_\theta^2}{r} = \frac{(vz - wy)^2}{r^3} \tag{19}$$

Then, to update the density(ρ_b) by using the following isentropic relation.

$$\rho_b = \left(\frac{p_b}{p_i}\right)^{\frac{1}{\gamma}} \rho_i \tag{20}$$

where p_i is the static pressure and ρ_i is the density at the first interior cell of the outlet boundary. The total energy is updated based on p_b and ρ_b.

On the solid wall, the non-slip boundary condition is applied to enforce mass flux going through the wall to be zero. The velocity components of the ghost cells are obtained by the extrapolation between the moving wall velocity and interior cells as follows:

$$\vec{V_b} = 2\vec{V_w} - \vec{V_i} \tag{21}$$

where $\vec{V_b}$ denotes the ghost cell velocity, $\vec{V_i}$ stands for the velocity of $1st$ interior cell close to the wall, and $\vec{V_w}$ is wall moving velocity given by $\vec{\Omega} \times \vec{r}$. Another option to save mesh size in our computation is to use the law of the wall. When y^+ is between 11 and 300, the no slip condition is replaced by using the wall function.

$$u^+ = \frac{1}{k} ln y^+ + B \tag{22}$$

where k denotes Von Kármán constant taken as 0.41, and B denotes a dimensionless constant corresponding to the wall roughness taken as 5.0. If the wall surface is η direction, the wall static pressure for the inviscid momentum equation can be determined by solving Eq. (19) in the following manner:

$$\frac{\partial p}{\partial \eta} = \frac{\rho_i}{\sqrt{\eta_x^2 + \eta_y^2 + \eta_z^2}} \frac{V_\theta^2}{r} \tag{23}$$

If the wall surface is stationary, then the static pressure gradient across the wall boundary is set to zero. For addition, the adiabatic condition($\partial T/\partial \eta = 0$) is used to impose zero heat flux through the wall.

Downloaded by Gecheng Zha on March 3, 2017 | http://arc.aiaa.org | DOI: 10.2514/6.2017-0783

4 Structural Model

For the rotating blades in the relative frame of reference, on can assume that the stiffness of the rotor disk is much larger than that of the compressor blades, the vibration characteristics of the blades is dominant such that rotor disk vibration effects are negligible. The center of the rotor disk is aligned to the rotating axis, as a result no whirling effects exist. No translational acceleration of arbitrary frame of reference to absolute frame and constant rotational speed are considered.

4.1 Modal Approach

The equation of motion of an N-DOF(degree of freedom) system with the mechanical damping and the aerodynamic loading as the excitation force can be presented in matrix form:

$$[\mathbf{M}]\{\ddot{\mathbf{X}}\} + [\mathbf{C}]\{\dot{\mathbf{X}}\} + [\mathbf{K}]\{\mathbf{X}\} = \{\mathbf{F}\} \tag{24}$$

where, **M**, **C**, **K** are the mass, structural damping and stiffness matrices. **F** is total aerodynamic force acting on the blade surface. Total aerodynamic force can be defined as follows:

$$\mathbf{F} = -\oint P \cdot \hat{n} dA + \oint \tau_{\mathbf{w}} \cdot \hat{t} dA \tag{25}$$

where, $\hat{n}$ is the unit normal vector to the blade surface and $\hat{t}$ is the unit tangent vector to the blade surface. P is the fluid static pressure and $\tau_{\mathbf{w}}$ is the fluid wall shear stress acting on the blade surface. Eq. (9) is used to compute static pressure of rotor blade surface by setting flow velocity components to zero. It is likely that the effects of viscosity may not be neglected for the highly loaded transonic rotor because rotating stall with large structure of flow separation may occur in/near stall conditions.

To decouple the equations of motion for the damped systems(24), we use the mass normalized mode shape($\tilde{\phi}$) defined as the normal modes divided by square root of the the generalized mass($\sqrt{\phi^T m \phi}$). Let $\{\mathbf{X}\} = [\tilde{\Phi}]\{\mathbf{q}\}$ and premultiply Eq. (24) by the transpose $[\tilde{\Phi}]^T$.

$$\begin{aligned}[\tilde{\Phi}]^T[\mathbf{M}][\tilde{\Phi}]\{\ddot{\mathbf{q}}\} + [\tilde{\Phi}]^T[\mathbf{C}][\tilde{\Phi}]\{\dot{\mathbf{q}}\} + [\tilde{\Phi}]^T[\mathbf{K}][\tilde{\Phi}]\{\mathbf{q}\} \\ = [\tilde{\Phi}]^T\{\mathbf{F}\}\end{aligned} \tag{26}$$

where **q** is the vector of the principal coordinates. By the orthogonality of the system matrices and assuming damping matrix to be a linear combination of the mass and stiffness matrices, Eq. (26) is then completely decoupled and jth equation will have the form

$$\ddot{q}_j + 2\zeta_j \omega_j \dot{q}_j + \omega_j^2 q_j = \frac{\tilde{\phi}_j^T}{m_j}\mathbf{F} \tag{27}$$

where $[\tilde{\Phi}]^T = [\tilde{\phi}_1, \cdots, \tilde{\phi}, \cdots, \tilde{\phi}_N]^T$. N is the number of modal coordinates. ω_j and ζ_j are natural frequency and modal damping ratio for mode j. m_j denotes the jth diagonal element of modal mass matrix which will be unity. In the current study, the structural system may be reduced to only five mode shapes, since a few bending and torsional frequencies are usually sufficient to determine flutter. The normalized modal equation can be given as

$$\ddot{q}_j + 2\zeta_j(\tfrac{\omega_j}{\omega_\alpha})\dot{q}_j + (\tfrac{\omega_j}{\omega_\alpha})^2 q_j = \frac{\tilde{\phi}_j^{*T}}{m_j^*} \cdot \mathbf{F}^* \cdot {V_f}^2 \cdot \frac{b_s^2 L_\infty}{V} \cdot \bar{m} \tag{28}$$

where the dimensionless quantities are denoted by an asterisk. $V_f(= \frac{U_\infty}{b_s \omega_\alpha \sqrt{\bar{\mu}}})$ is the flutter speed index which is an input flutter control parameter. $\bar{m}$ is the measured blade mass, $\bar{V}$ represents the conical frustum volume and b_s is the streamwise root semi chord. L_∞ is the reference length and ω_α is the angular frequency of the first torsional mode in units $radians/sec.$ $\bar{\mu}(= \frac{\bar{m}}{V\rho_\infty})$ stands for the mass ratio, i.e. the ratio between the structural mass and the mass of the equivalent volume of fluid at reference density. It is noticed that m_j^* should equal one when the mass normalized mode shapes are used.

The equations are then transformed to a state form as follows:

$$[\mathbf{M}]\frac{\partial \mathbf{S}}{\partial t} + [\mathbf{K}]\{\mathbf{S}\} = \mathbf{q} \tag{29}$$

where

$$\mathbf{S} = \begin{pmatrix} q_j \\ \dot{q}_j \end{pmatrix}, \mathbf{M} = [I], \mathbf{K} = \begin{pmatrix} 0 & -1 \\ (\frac{\omega_j}{\omega_\alpha})^2 & 2\zeta_j(\frac{\omega_j}{\omega_\alpha}) \end{pmatrix}$$

$$\mathbf{q} = \begin{pmatrix} 0 \\ \phi_j^{*T} \cdot \mathbf{F}^* \cdot V_f \cdot \frac{b_s^2 L}{\bar{V}} \cdot \bar{m} \end{pmatrix}$$

Downloaded by Gecheng Zha on March 3, 2017 | http://arc.aiaa.org | DOI: 10.2514/6.2017-0783

4.2 Implicit Structural Solver

To solve the structural equations with CFD solver in the fully coupled manner, the decoupled structural equations are integrated in a manner consistent with flow governing equations each physical time step :

$$\begin{aligned}&\left(\frac{1}{\Delta\tau}I+\frac{1.5}{\Delta t}M+K\right)\delta S^{n+1,m+1}\\&=Q^{n+1,m+1}-M\frac{3S^{n+1,m}-4S^{n}+S^{n-1}}{2\Delta t}-KS^{n+1,m}\end{aligned}\tag{30}$$

The fluid/structural interaction is implemented in a fully coupled manner[15]. Within each physical time step, the flow equations and structural equations are solved iteratively until the prescribed convergence criteria is satisfied for both flow and structural solver. After the convergence criteria is reached, the fluid-structural interaction goes to next physical time step.

4.3 Rotor-Stator Interface Sliding Boundary Conditions

For unsteady rotor-stator interaction simulation, the rotor mesh will rotate with the rotor blades and the stator mesh will be stationary. Solving the Navier-Stokes equations requires transferring the fluxes between these two meshes. In [27], a conservative sliding BC is developed by making the meshes on both side of the sliding boundary one-to-one connected. Even though the conservative BC is mathematically more rigorous, it is not convenient to make the mesh one-to-one connected. For engineering applications, independent mesh for rotor and stator is desirable for efficient setup of a simulation. This paper thus adopts an interpolation sliding BC with high accuracy to remove the requirement that the rotor and stator mesh needs to be one-to-one connected.

The working mechanism of present interpolation rotor/stator sliding BC is sketched in Fig. 2, where S1, S2, S3, S4 and R1, R2, R3 are the arbitrary computational mesh cells of the stator and rotor in the circumferential direction on the two sides of the sliding interface. The current interpolation sliding boundary condition is based on the same grid radial distribution of the mesh on both side of the sliding boundary.

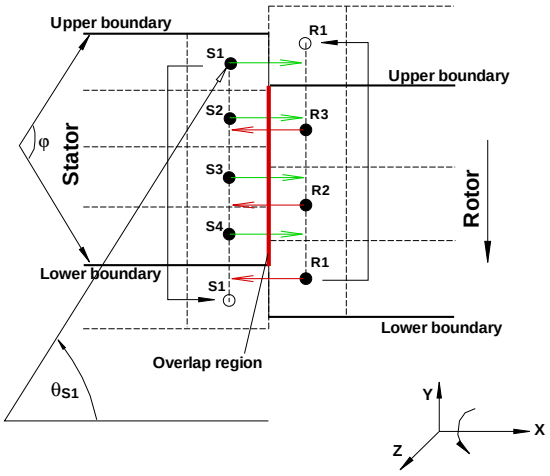

Figure 2: Working mechanism of interpolation rotor/stator sliding BC

To interpolate the conservative variable vector $\mathbf{Q}$, the circumferential mesh angle is first obtained at each mesh cell center, e.g. the angle of a stator cell s1, θ_{s1} can be defined as $tan^{-1}(z/y)_{s1}$. Then, two

Downloaded by Gecheng Zha on March 3, 2017 | http://arc.aiaa.org | DOI: 10.2514/6.2017-0783

adjacent mesh angles in the opposite interface corresponding to current mesh cell are found for linear interpolation, e.g. $\mathbf{Q}$ at R3 is interpolated in terms of $(\theta_{R3} - \theta_{S2})$ and $(\theta_{S3} - \theta_{S2})$ as given in Eq. (31). Note that a rotation rule based on the geometric periodicity is used to interpolate $\mathbf{Q}$ in the non-overlap region, e.g. $\mathbf{Q_{S1}}$ is rotated by the periodic sector angle (φ) to interpolate $\mathbf{Q_{R1}}$ vice versa for $\mathbf{Q_{R1}}$.

$$\mathbf{Q}_{R3} = \frac{\theta_{R3} - \theta_{s2}}{\theta_{s3} - \theta_{s2}}(\mathbf{Q}_{s3} - \mathbf{Q}_{s2}) + \mathbf{Q}_{s2} \tag{31}$$

Since the frame of reference taken in this study is a fixed frame for the stationary blades and a moving relative frame for the rotor, the following exchange relations between the fixed and moving relative frame are used.

$$\begin{pmatrix} \rho \\ \rho u \\ \rho v_r \\ \rho(v_\theta + rR_o) \\ \rho(e + c_\theta r R_o) \end{pmatrix}_{Fixed} \rightleftharpoons \begin{pmatrix} \rho \\ \rho u \\ \rho v_r \\ \rho v_\theta \\ \rho e \end{pmatrix}_{Moving} \tag{32}$$

5 Mesh and Mode Shape

The transonic axial compressor, NASA stage 35 that consists of 36 rotor blades and 46 stator blades[28], is simulated to investigate the stall inception mechanism using the interpolation rotor/stator sliding BC. The total pressure ratio of NASA stage 35 at design speed of 17189 rpm is 1.82. Full annulus of stage 35 is simulated and a partial mesh is shown in Fig. 3. An O-mesh topology around blades and H-mesh for stage inlet/outlet duct region are used. The inlet and outlet duct are extended by 8 times of rotor chord length to form non-reflecting boundary conditions. Total mesh points of the half annulus are 18696870 with 482 blocks. The rotor tip clearance is modeled using a fully gridded O-mesh. In the tip gap, 11 grid points are placed radially. The physical time step size is determined to allow about 20 unsteady steps per rotor blade passing.

The blade structure is modeled by its first 5 natural vibration mode shapes generated by using commercial solver ABAQUS. The design rotating speed is 17188.7 rpm. The blade is made of Maraging200 with a density of 8200 kg/m3 approximately. Fig. 4 shows the 1st to 5th mode shapes. The blades are modeled as fixed at the rigid body rotor and the centrifugal force is considered in mode extrapolation. The mass ratio between the blade and air is about 7528. This rotor is selected because the geometry and material data is available in the public domain.

6 Results and Discussion

The simulations start with the unsteady calculation of the flow field of the stationary rigid blade. After the unsteady flow field is fully developed, the rigid blades are switched to the flexible blades.

6.1 Code Validation

Fig. 5 shows the predicted speedline for NASA Stage 35 using steady state single blade passage with mixing plane boundary condition on the rotor and stator interface. A refined mesh of total 550,750 grid points and a baseline mesh (main mesh) of 449,790 grid points per blade passage are used for the mesh refinement study using the mixing plane[27]. The speedline predicted by the two meshes shows good agreement. Therefore, the baseline mesh is used to construct the full annulus mesh in Fig. 3. The simulation is conducted at 4004 test condition[28](Point A) since the measured radial profiles for CFD

Downloaded by Gecheng Zha on March 3, 2017 | http://arc.aiaa.org | DOI: 10.2514/6.2017-0783

Downloaded by Gecheng Zha on March 3, 2017 | http://arc.aiaa.org | DOI: 10.2514/6.2017-0783

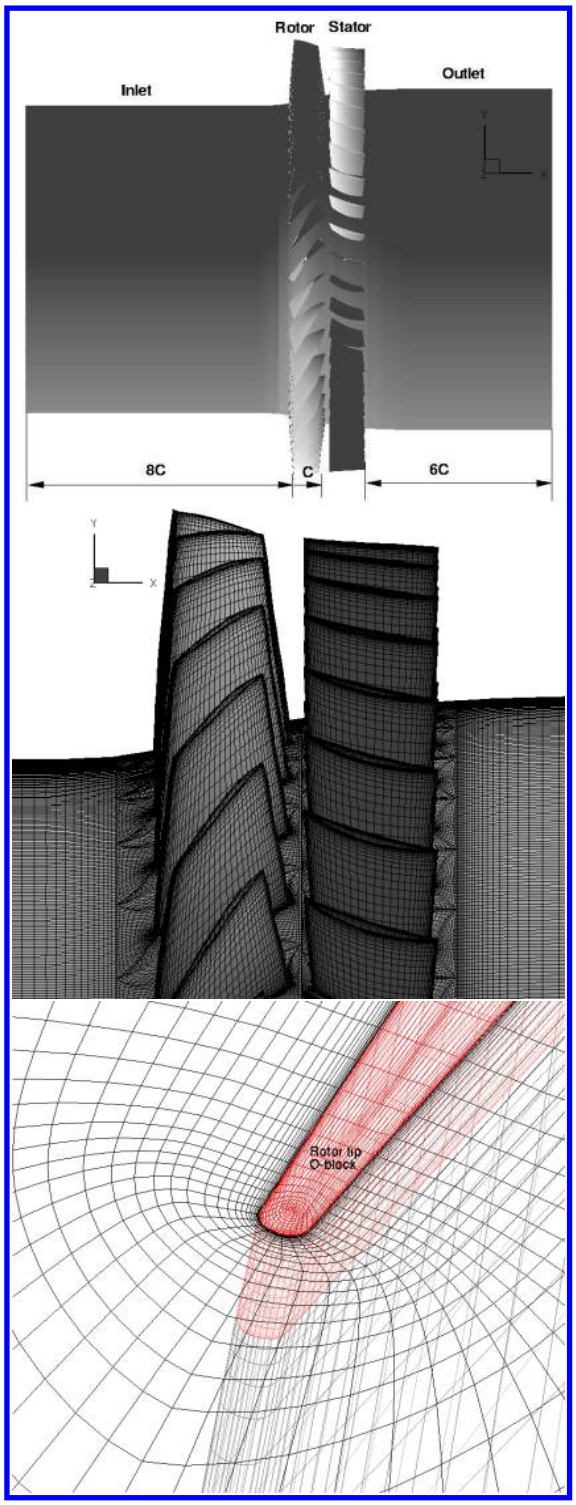

Figure 3: Full annulus mesh of NASA stage 35

comparison are available. The mass flows at choke condition predicted by both unsteady rotor/stator interaction and steady mixing plane are about 20.82 kg/s, which is about 0.62% lower than the measured choke flow of 20.95 kg/s[28]. The unsteady flow and FSI simulation start point B.

The circumferential mass averaged total pressure ratio, total temperature ratio, adiabatic efficiency and absolute flow angle at stage outlet are compared with the measurement at 4004 point[28] in Fig. 6. Overall good agreement with the experiment is achieved by both the mixing plane and the interpolation

Downloaded by Gecheng Zha on March 3, 2017 | http://arc.aiaa.org | DOI: 10.2514/6.2017-0783

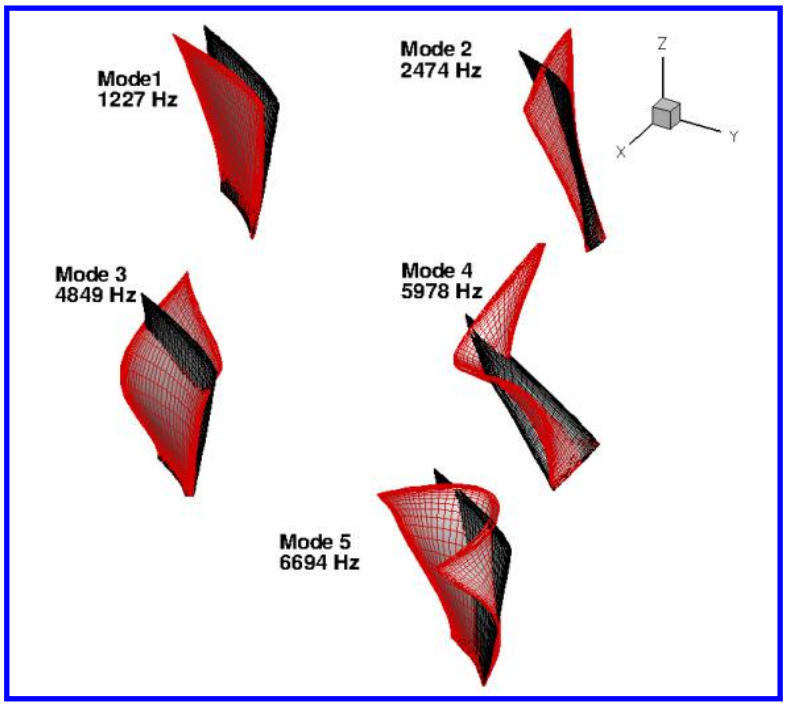

Figure 4: Mode shape of Rotor 35

rotor/stator sliding BC.

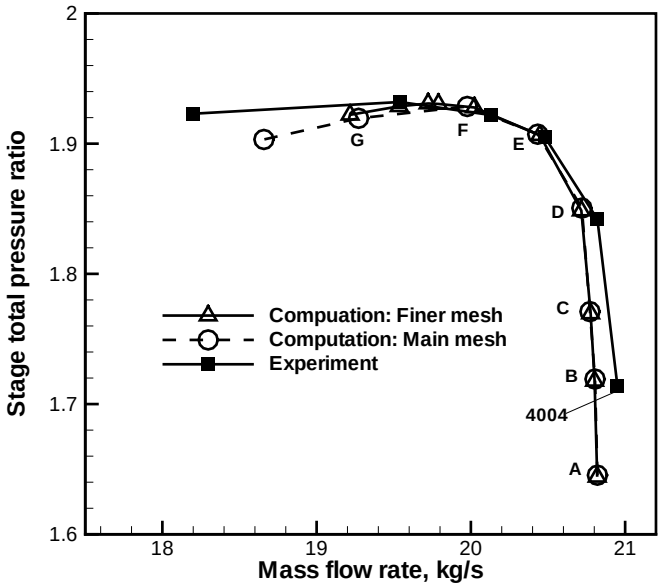

Figure 5: Predicted speedline of NASA stage 35

Fig. 7 shows the instantaneous entropy contours calculated by the unsteady simulation at mid span of the compressor at point B. The wake propagates through the rotor/stator interface smoothly. Fig. 8 compares the instantaneous normalized mass flux ρU (top) and static pressure P (bottom) right upstream and downstream of the interface, which indicates excellent flux conservation through the rotor/stator interface by the interpolation BC.

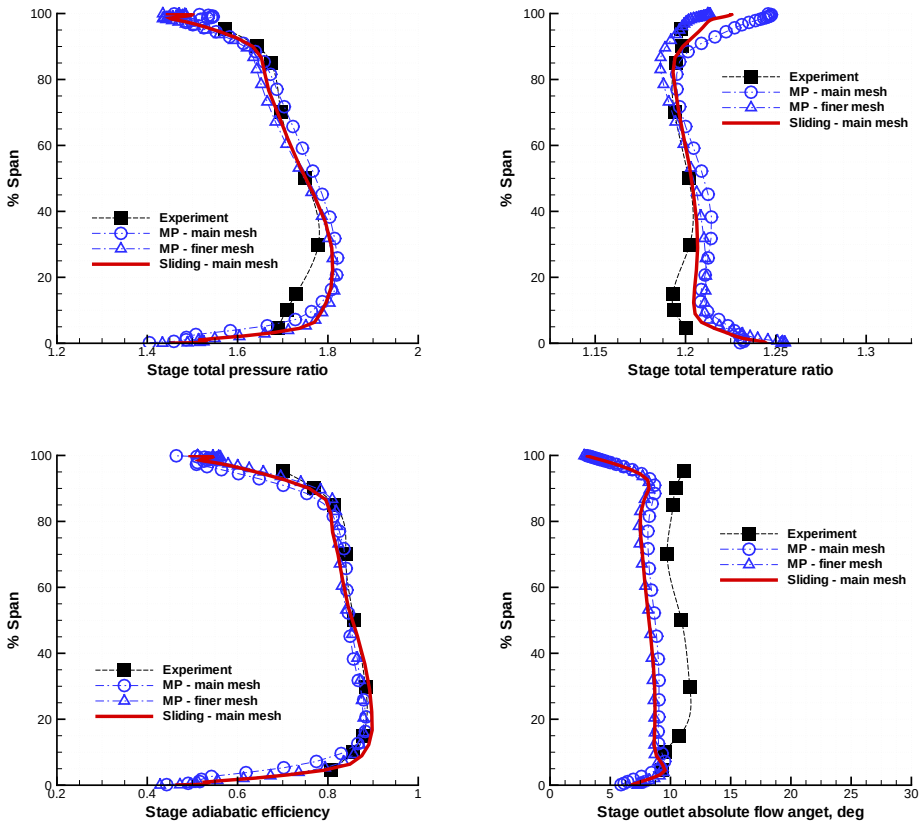

Figure 6: Predicted pitch averaged radial profiles at 4004 including stage total pressure ratio, total temperature ratio, adiabatic efficiency and outlet absolute flow angle

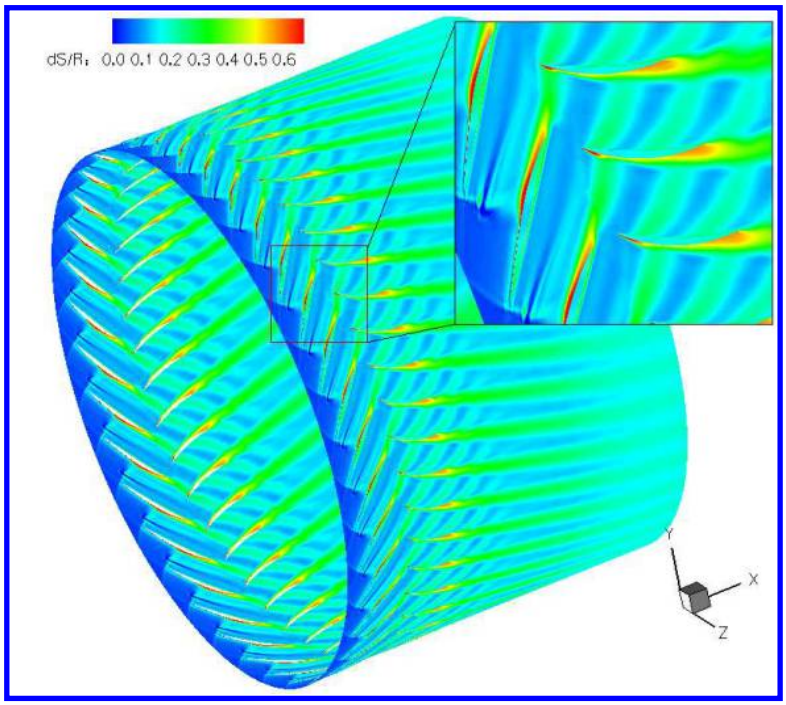

Figure 7: Instantaneous entropy contour at mid span of NASA stage 35

Downloaded by Gecheng Zha on March 3, 2017 | http://arc.aiaa.org | DOI: 10.2514/6.2017-0783

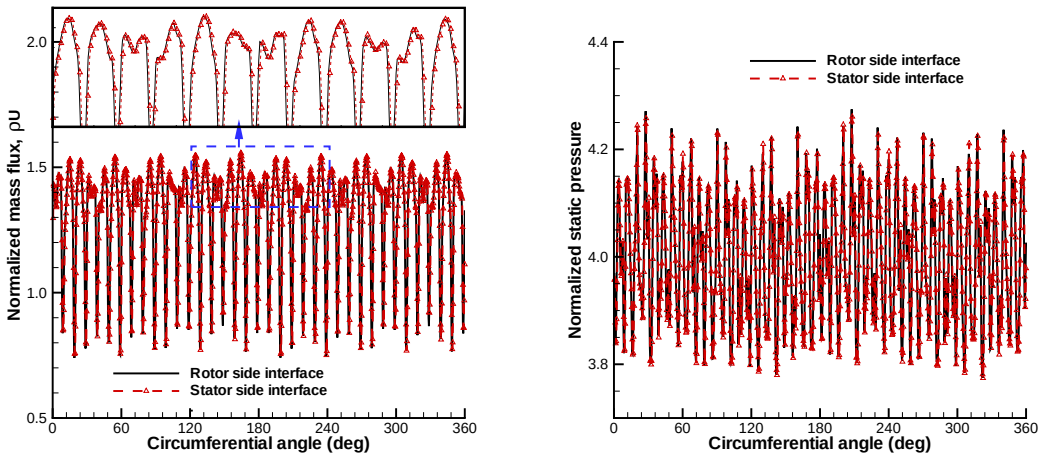

Figure 8: Instantaneous normalized mass flux ρU (left) and static pressure P (right) at mid span of the rotor/stator interface

Downloaded by Gecheng Zha on March 3, 2017 | http://arc.aiaa.org | DOI: 10.2514/6.2017-0783

6.2 Stall Flutter Boundary

The unsteady simulations with rigid blades are first conducted to determine the exact stall point of the compressor. It is found that the compressor begin to stall from point E[29]. The development of the rotating stall of Stage 35 is shown in Fig. 9. In the plot, the time history of static pressure around the full annulus is shown. Rotating stall is usually initiated from rotor tip. To capture the rotating stall, the numerical probes are hence located about 50% tip chord length upstream and downstream at the rotor tip span. The static pressures are from those numerical probes. At about 14.5T, a spike like disturbance traveling with full rotor speed is seen. The stall cell speed can be determined by the slope of pressure/velocity propagation versus time. The spike disturbance continues to rotate and and propagate to more blade passage with about 90% rotor speed. After 1.5T, the stall cells propagation slows down to 50% of the rotor speed in the opposite direction of the rotor rotation. The rotating stall is fully developed within 1.2 rotor revolutions.

The FSI simulations start from a converged unsteady flow results. Because the stall flutter usually occurs near stall point, the back pressures are adjusted along the speedline as shown in Fig. 5 for point B, C, D and E to see if the flutter exists. As a small imposed initial perturbation, all the five modes of the blade structural motion are given the same normalized initial velocity, which is 1.0e-6. Then the blades are allowed to deflect in response to the dynamic force load. Within each physical time step, the solution is usually converged with 20-30 iterations. Fig. 10 shows the variations of mass flow rate during rotating stall with FSI simulation. It can be seen that the mass flow drops slowly up to 1.0 revs and decrease quickly after that in the calculation starting from point E. It is noted that the compressor stall begins earlier in the unsteady simulation than that in steady simulation, in which the compressor stall start near point F. The reason may be that the unsteady simulation predicts more total pressure loss than the steady simulation. The mass flow rate is dynamically stable at point D.

The time history of the first 5 modal displacements with a backward traveling wave of ND=1 at condition point C is shown in Fig. 11. Zero structural damping ratio has been used in the calculation. The response of the first mode increases gradually, while the other modes decay with time. The first mode is dominant since the amplitude of the first mode is about 4 times higher than that of the second mode. The response of the first mode at working conditions of point B, C, D and E are compared in Fig. 12. It can be seen that the amplitudes of the first mode at all conditions diverged gradually, which indicates that the predicted response is flutter in the first mode without structural damping. As the working point shifting from near peak condition (point D) to stall condition (point E), the vibration

amplitude increase. The highest amplitude of blade vibration occurs at point E and the response become chaotic due to the rotating stall flow acting on the blade surface, which is not periodic.

Turbomachinery blade flutter often involves traveling wave in which the blades vibrate at the same frequency but with a constant phase difference termed as inter blade phase angle. The numbers of nodal diameter is not known until the engine is made and tested. The modal displacements with different inter blade phase angle in backward traveling mode is shown in Fig. 14. The results in the plot are used zero structural damping coefficient at point C. It is shown that the amplitude of the 1st mode decreases as the number of ND is increased. In other words, the phase angle of ND=1 is the least stable condition. Fig. 15 shows the generalized displacement for all the blades. It can be seen that the traveling waves with ND of 1 and 2 are clearly captured.

The structural damping is a very important parameter, but is difficult to obtain from experiment. The structural damping value of the blades in NASA Stage 35 is not available, so all the structural damping coefficients used in the calculation are set with empirical values. The modal displacement of the 1st mode with different damping coefficient are shown in Fig. 12. It can seen that the vibration amplitude decrease as the structural damping increase. Fig. 13 shows the response of the 1st mode with damping value of 0.003 at different working conditions. It is observed that the vibration damped quickly with this higher damping coefficient at all points except at point E. The response of point E damped in the first three rotor revolutions and diverged after that. The Stage 35 start stall near point E. It appears that the stall flutter in Stage 35 is due to the rotating stall.

The DDES method is more capable of predicting vortical than URANS, so DDES is also conducted at rotating stall point E. The predicted modal displacements of the 1st mode by using both URANS and DDES are shown in Fig. 16. It can be seen that both methods predicted damped responses in the first 2 rotor revolutions. The response predicted by URANS begin to diverge after 3.5 rotor revolutions. And the amplitude of the 1st mode predicted by DDES begin to diverged after 2.5 rotor revolutions. The amplitude of vibration predicted by DDES is higher than that of URANS. The DDES method predict more energetic flow structure than the URANS method. The onset of rotating stall in the results of DDES starts earlier than that of URANS.

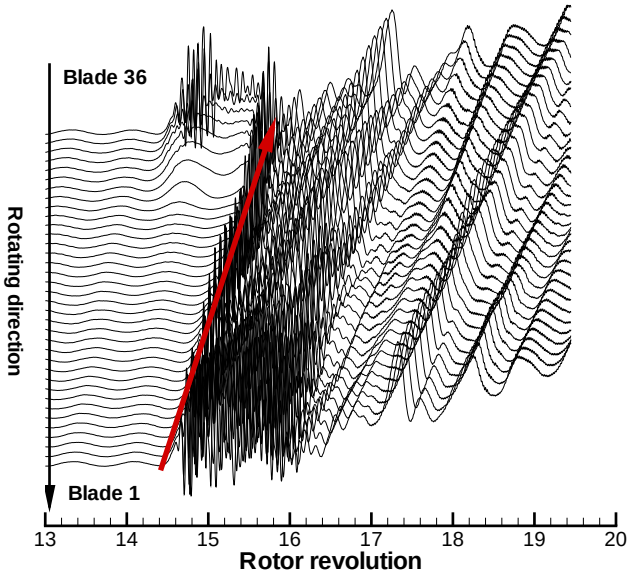

Figure 9: Variations in static pressure across tip span

Downloaded by Gecheng Zha on March 3, 2017 | http://arc.aiaa.org | DOI: 10.2514/6.2017-0783

Downloaded by Gecheng Zha on March 3, 2017 | http://arc.aiaa.org | DOI: 10.2514/6.2017-0783

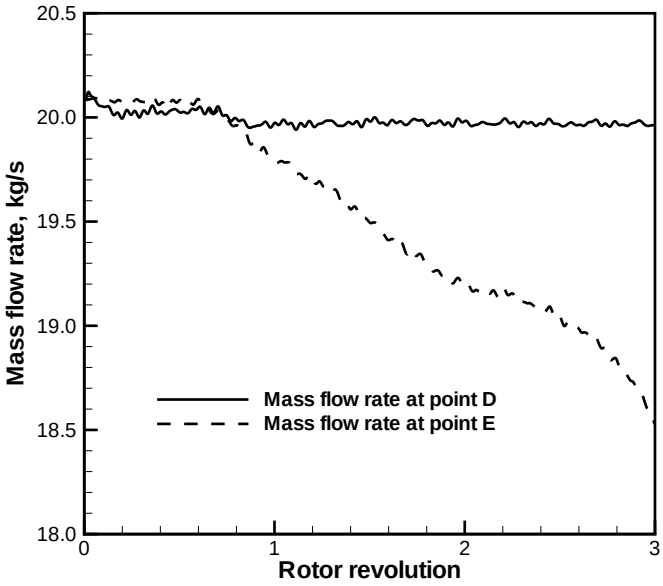

Figure 10: Mass flow variation during blade vibration

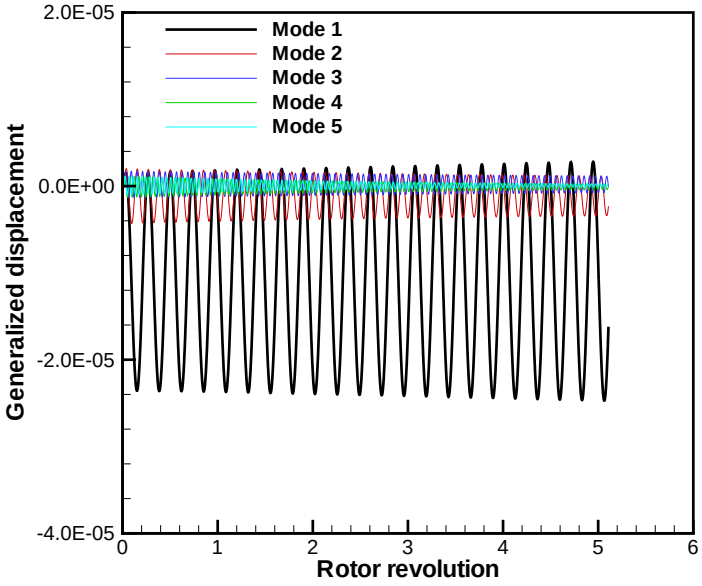

Figure 11: Modal displacements with ND=1 and zero structural damping at point C

6.3 Mechanism of Stall Flutter

Without damping

Simulations are conducted at stable condition point C with 2 nodal diameters and zero structural damping. Hence, all the damping in the structural response will be from the aerodynamic damping. The blade vibration is unstable with these input parameters as shown in Fig. 14.

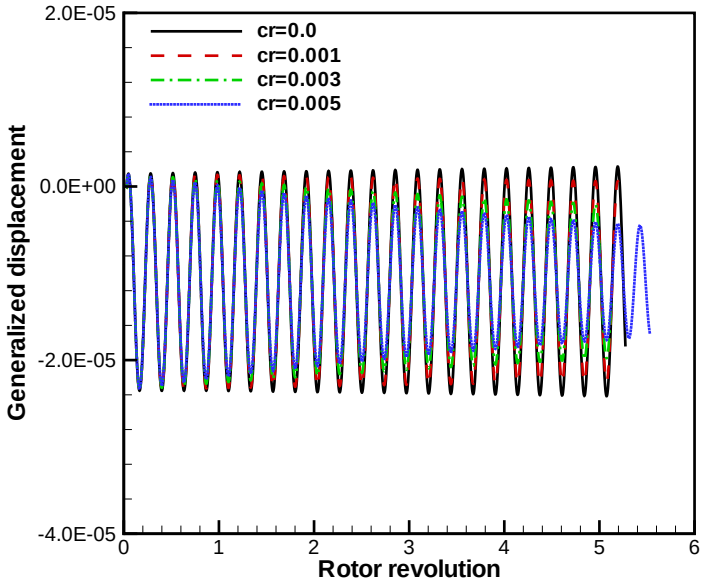

Figure 12: Blade 1st mode response with different structural damping and ND=1 at Point C

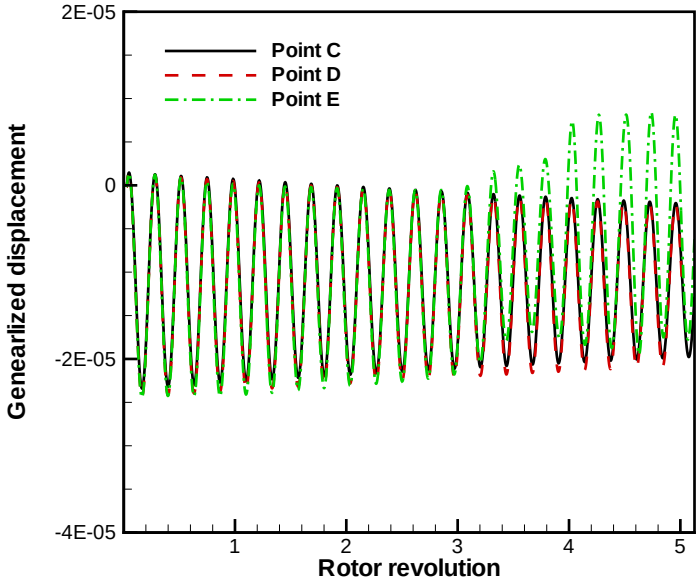

Figure 13: Blade 1st mode response with ND=2 at different working points

Fig. 17 shows the modal force and modal displacement during flutter. The modal force and modal displacement is about in phase, which indicates an unstable condition. Fig. 18 shows the time histories of angular displacement and pressure during flutter. The unsteady pressure fluctuation is also about in phase with that of the angular displacement.

Fig. 19 shows the spectrum of angular displacement at the leading edge of rotor tip. The blade vibration is mainly in the first mode. The amplitudes of vibration of the other modes are less than

Downloaded by Gecheng Zha on March 3, 2017 | http://arc.aiaa.org | DOI: 10.2514/6.2017-0783

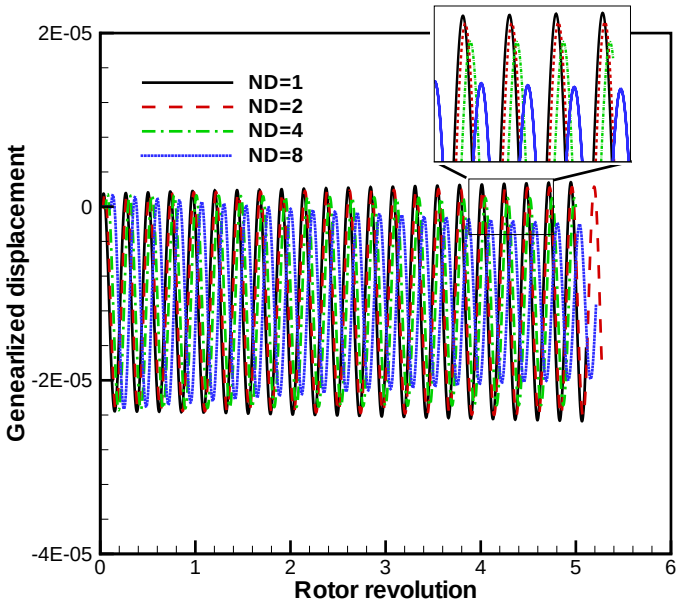

Figure 14: Blade 1st mode response with different nodal diameter at Point C

about three times of the first mode, which is consistent with the modal displacement as shown in Fig. 11. Fig. 20 shows the spectrum of static pressure at the leading edge of rotor tip. The dominant frequency is near the first natural frequency. Fig. 21 illustrates the pressure contours at point C during fluid structure interaction. The flow near rotor tip is periodic and steady. And shock waves is the dominant flow structure in blade passage.

With damping

The blade vibration is damped with the structural damping coefficient of 0.003 at all working points, except at point E. Fig. 22 shows the time history of mass flow rate at point E by using URANS and DDES. It can be seen that the predicted mass flow rate drops sharply after about 2 or 3 rotor revolutions with both URANS and DDES, which indicates the onset of rotating stall. Flow of DDES start about 2 rotor revolution earlier than that of URANS. The degree of mass flow fluctuation in DDES appears to be bigger than that in URANS, which may be the cause that the predicted amplitude of blade vibration of DDES is bigger than that of URANS as shown in Fig. 16.

Rotating stall in Stage 35 starts from rotor tip, hence the onset of rotating stall is sensitive to the flow perturbation near the tip region. The interaction of tip leakage flow with tip vortex can shift the onset of stall at lower back pressure. Fig. 23 shows the variations of instantaneous static pressure at half rotor tip upstream of the rotor at point E by using URANS and DDES. Due to the blade vibration, rotating stall appears to be triggered at about the same time like a modal inception as shown in the results of both URANS and DDES. The rotating stall simulation of rigid blades shows that stall begins with a few passage as spike inception. Hence, The pressure fluctuation predicted by DDES appear to be more chaotic than that of URANS.

Fig. 24 illustrates the modal force and modal displacement of the first mode predicted by URANS with that of DDES during stall flutter. It is shown in the figure that modal force and modal displacement is out of phase to each other and the amplitudes of both time dependent variables decay before stall developed in the rotor passage. The modal force and displacement diverge when rotating stall appear. And their oscillations are in phase, which cause the rotor blades become unstable.

Downloaded by Gecheng Zha on March 3, 2017 | http://arc.aiaa.org | DOI: 10.2514/6.2017-0783

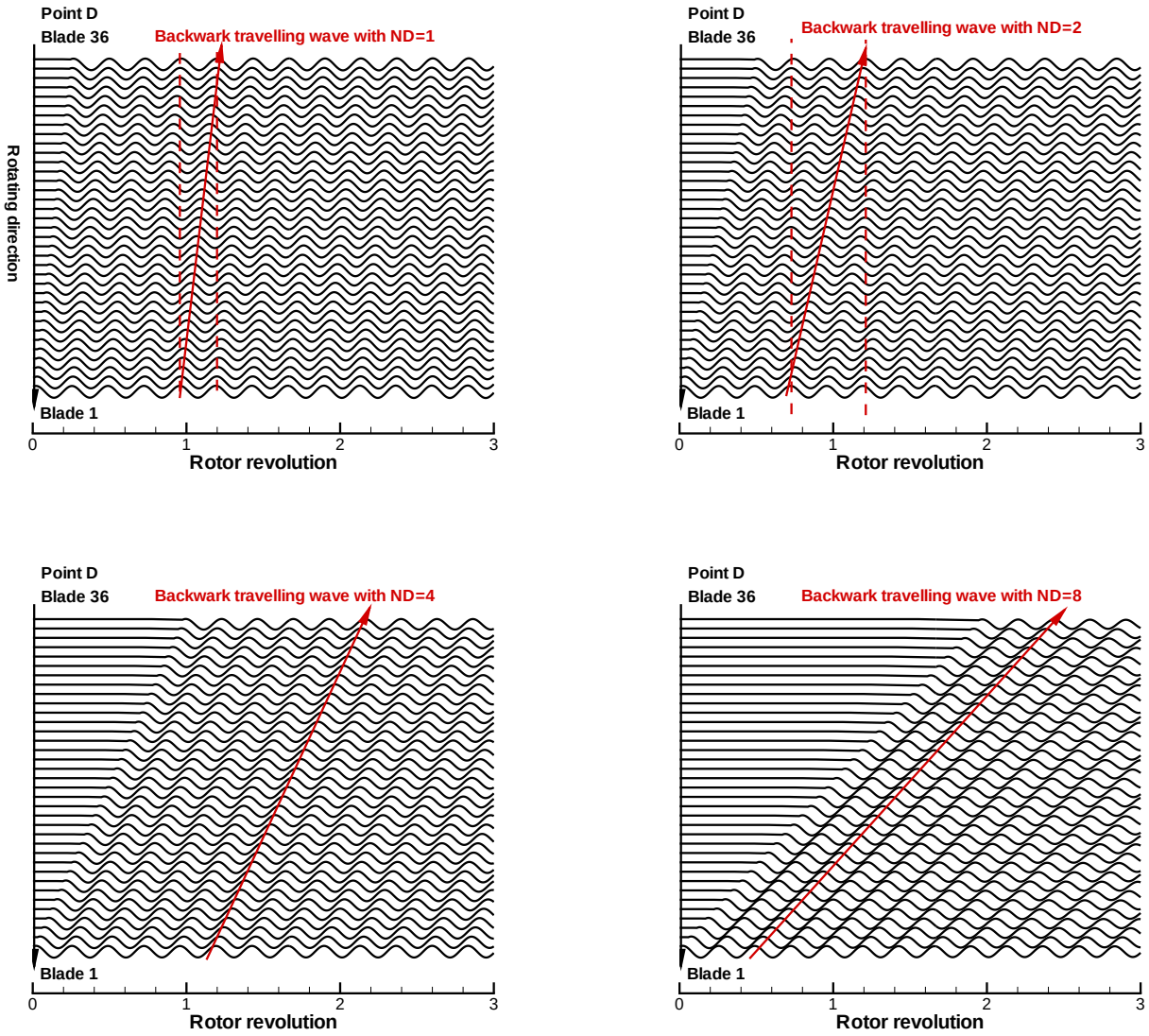

Figure 15: Predicted the backward traveling wave of 1st mode with a constant phase angle at point D

Fig. 25 shows the time histories of angular displacement and pressure near the leading edge of rotor tip during stall flutter. The variation of both parameters is similar to the modal force and displacement since the 1st mode is the dominant mode of the rotor blades.

Fig. 26 shows the spectrum of static pressure at the leading edge of rotor tip, in which the time series of samples are recorded from point E. It can be seen that both URANS and DDES capture similar unsteady flow behavior. For example, the highest amplitudes occurs at low frequency of around 200 Hz, and considerable fluctuation near the 1st natural frequency is captured. However, DDES predicts two dominant frequencies near the 1st natural frequency, where the URANS only has one. Fig. 27 shows the spectrum of angular displacement at the leading edge of rotor tip at point E. Both the URANS and DDES predict one dominant frequency near the 1st natural frequency.

Fig. 28 illustrates the pressure contours after 1 rotor revolution at the middle of tip clearance span. The flow predicted by both URANS and DDES in the stage is stable as shown in Fig. 22, so both flow modeling methods show similar pressure distribution. However, they become different each other after the stage in stall as shown in Fig. 29, which shows the pressure contours on the blade surface at 4 rotor

Downloaded by Gecheng Zha on March 3, 2017 | http://arc.aiaa.org | DOI: 10.2514/6.2017-0783

Downloaded by Gecheng Zha on March 3, 2017 | http://arc.aiaa.org | DOI: 10.2514/6.2017-0783

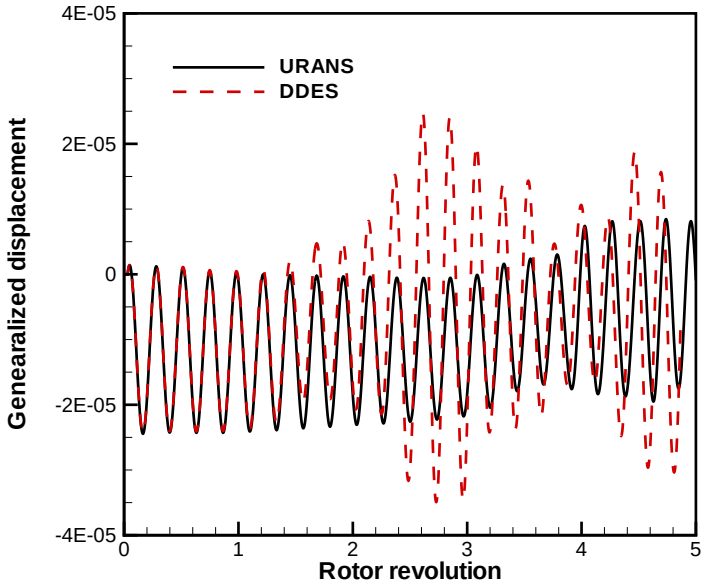

Figure 16: Predicted 1st mode displacements using DDES compared with URANS

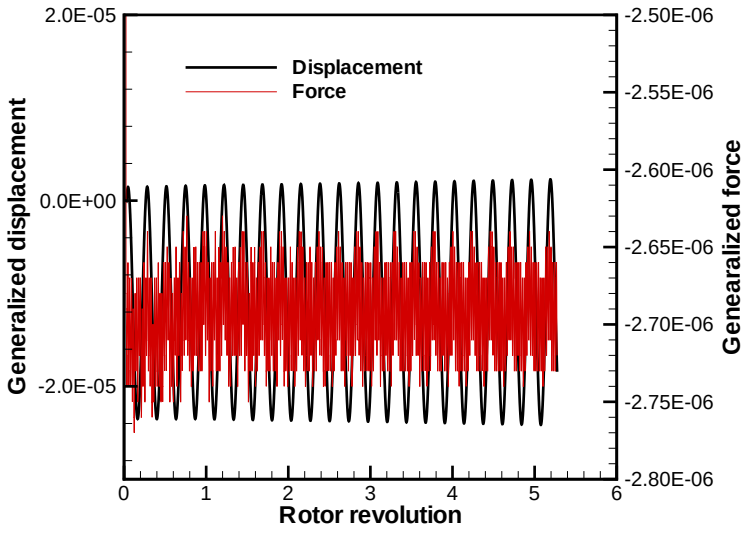

Figure 17: Modal displacement and force of 1st mode at point C with ND=2 and zero damping

revolutions. The flow blockage predicted by DDES is bigger than the URANS in both circumferential and streamwise directions. Fig. 30 shows the entropy distribution at cross section near rotor leading edge during rotating stall. The interaction between rotating stall cells and blades in DDES is more intense than that in URANS, which lead to higher amplitude of vibration of DDES compared with that of URANS. The large flow oscillation due to the flow blockage predicted by both DDES and URANS makes the blades absorbing more energy from the flow, which cause the rotor blades to vibrate unstably.

Downloaded by Gecheng Zha on March 3, 2017 | http://arc.aiaa.org | DOI: 10.2514/6.2017-0783

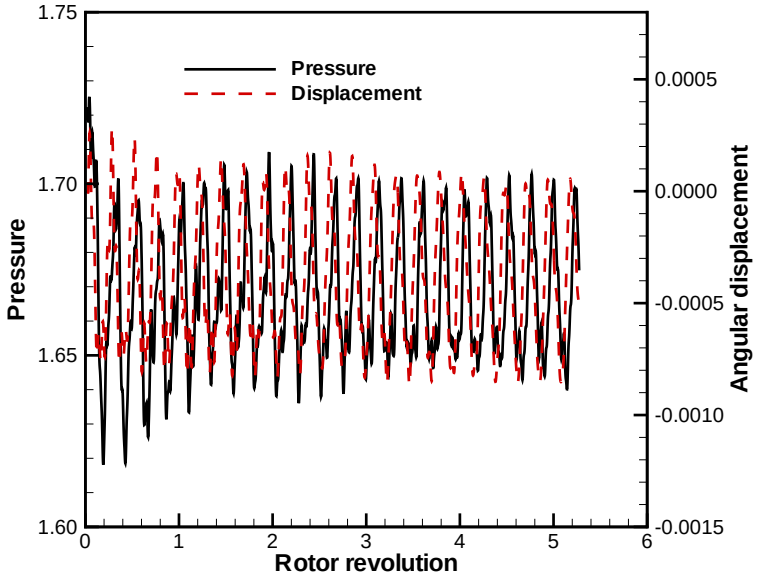

Figure 18: Time history of pressure and angular displacement at point C with ND=2 and zero damping

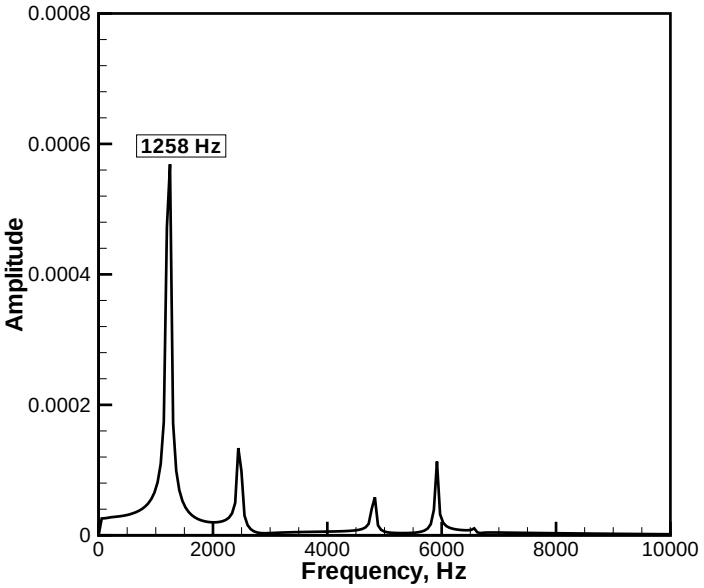

Figure 19: Spectrum of angular displacement near the leading edge at the rotor tip

Downloaded by Gecheng Zha on March 3, 2017 | http://arc.aiaa.org | DOI: 10.2514/6.2017-0783

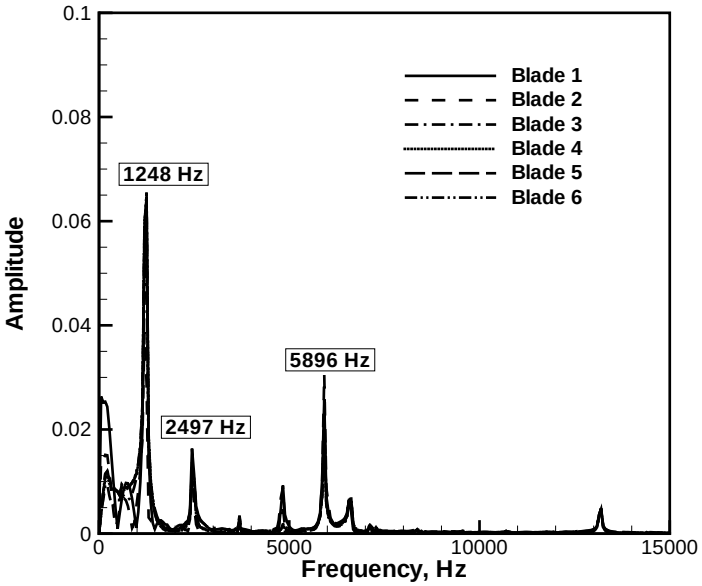

Figure 20: Spectrum of pressure near the leading edge at the rotor tip

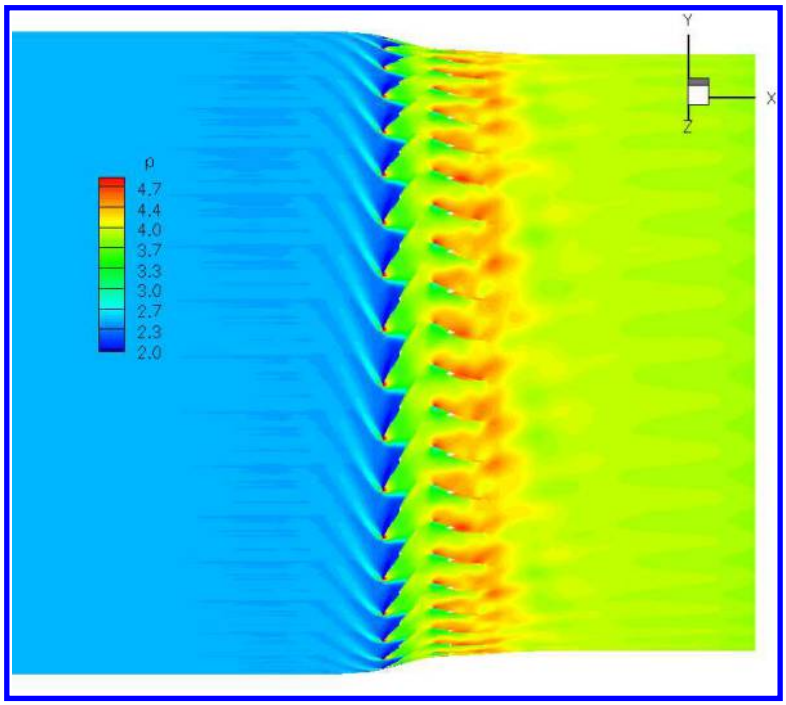

Figure 21: Pressure contour near tip span at time of 4 rotor revolution

Downloaded by Gecheng Zha on March 3, 2017 | http://arc.aiaa.org | DOI: 10.2514/6.2017-0783

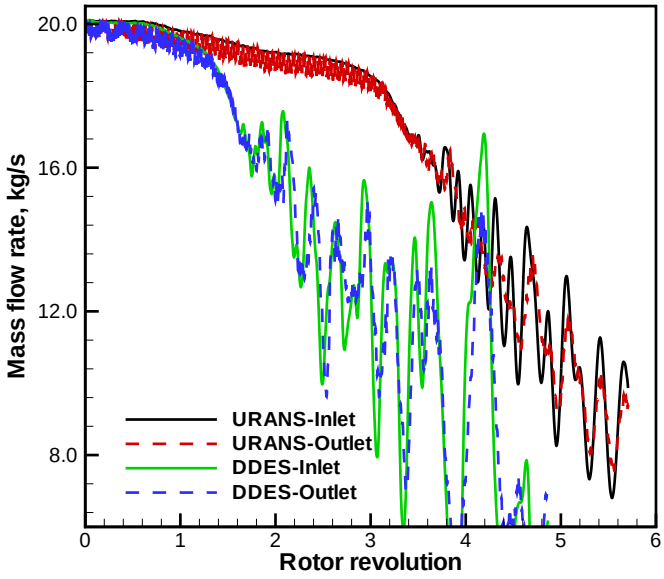

Figure 22: Time history of mass flow rate during stall flutter

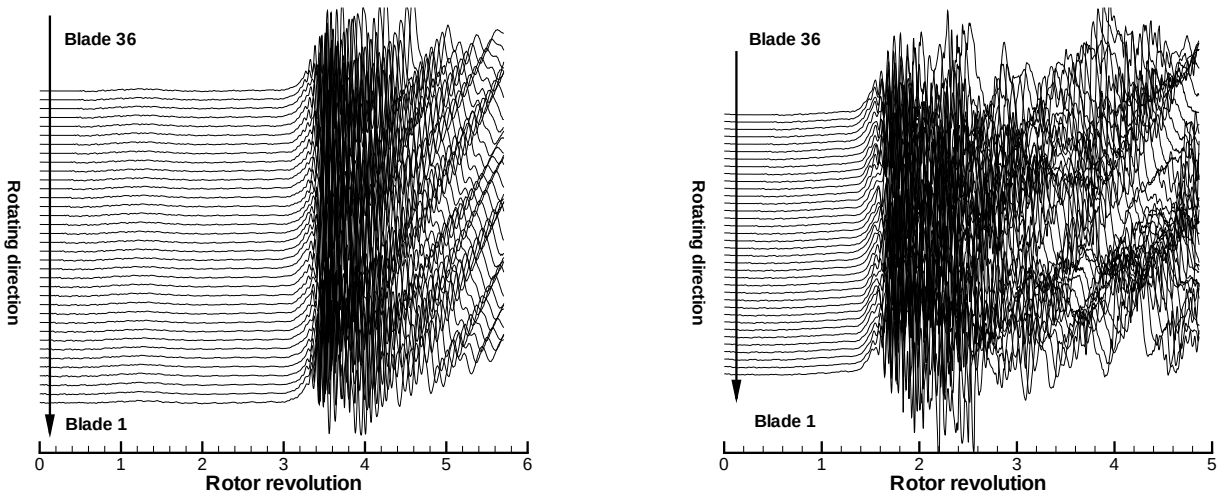

Figure 23: Time traces of pressure near half tip chord length upstream of the rotor leading edge at the tip span. Left: URANS, Right: DDES

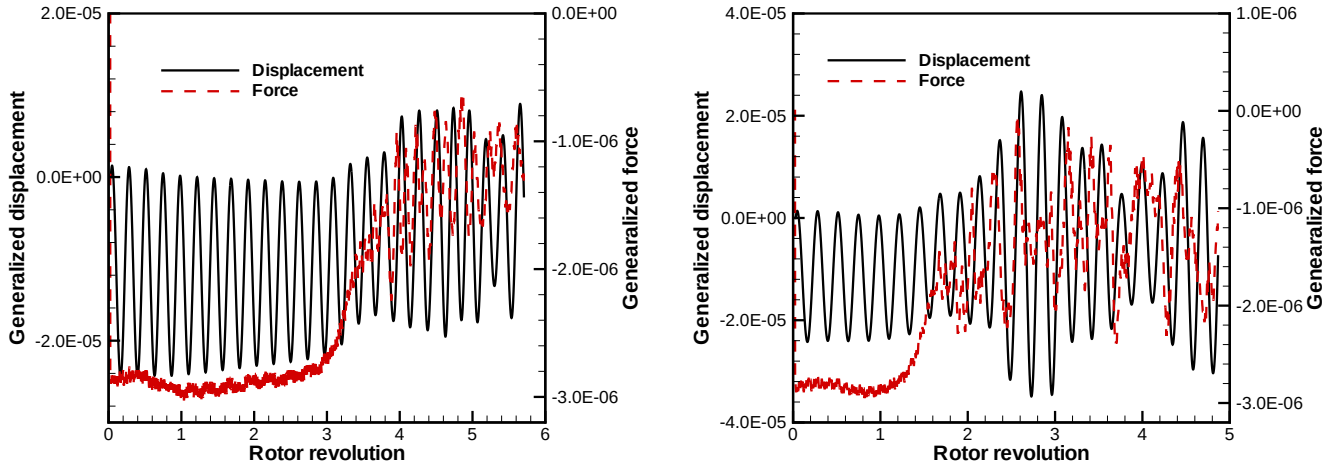

Figure 24: Modal displacement and force of 1st mode at point E with ND=2 and zero damping. Left: URANS, Right: DDES

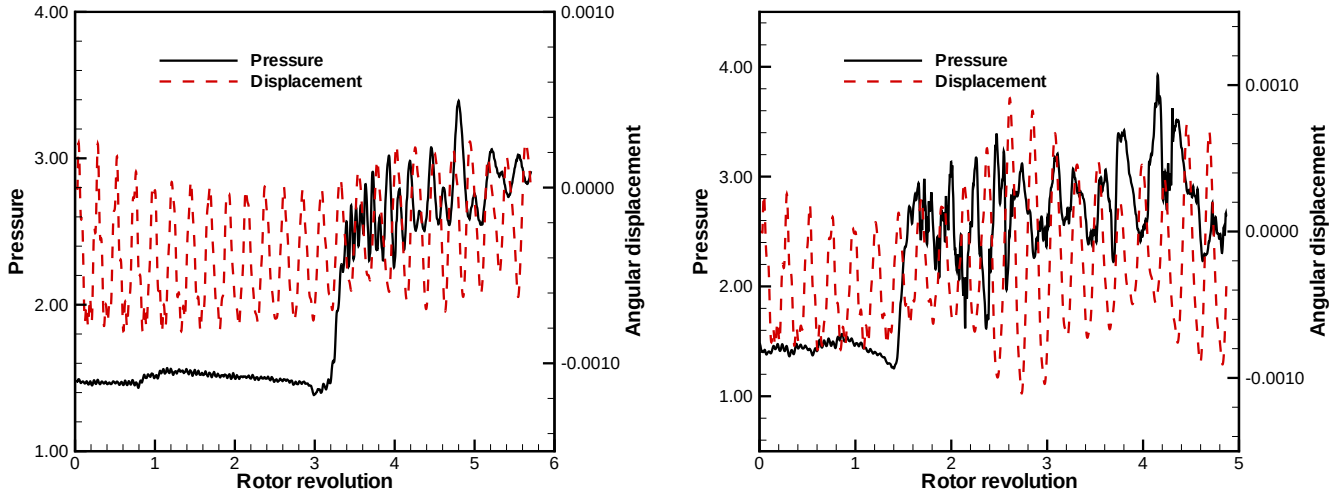

Figure 25: Time history of pressure and angular displacement at point E with ND=2 and zero damping. Left: URANS, Right: DDES

Downloaded by Gecheng Zha on March 3, 2017 | http://arc.aiaa.org | DOI: 10.2514/6.2017-0783

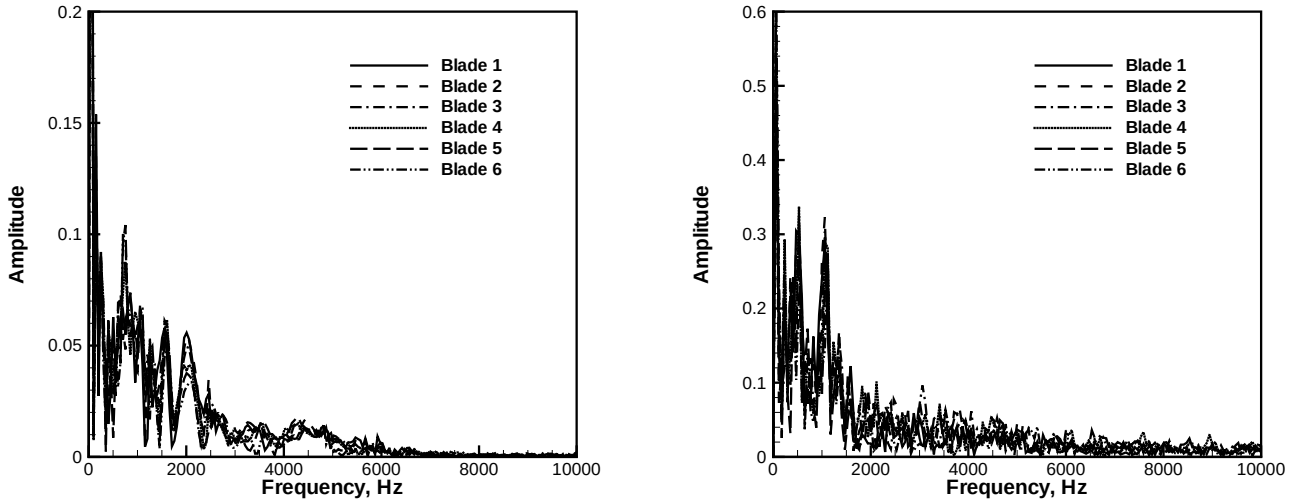

Figure 26: Spectrum of pressure near the leading edge at the rotor tip. Left: URANS, Right: DDES

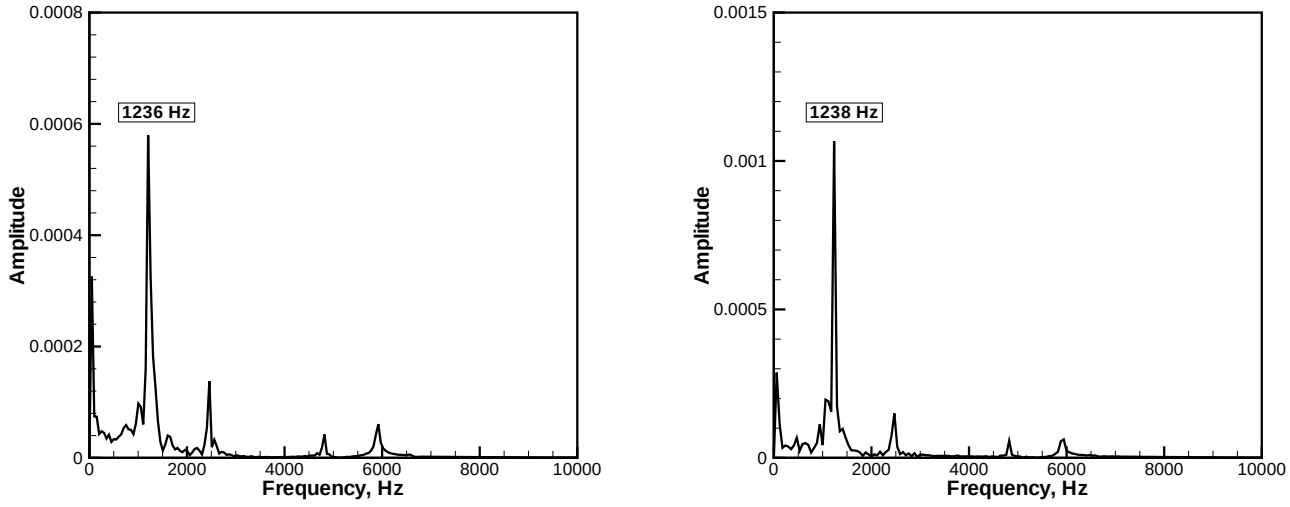

Figure 27: Spectrum of angular displacement near the leading edge at the rotor tip. Left: URANS, Right: DDES

Downloaded by Gecheng Zha on March 3, 2017 | http://arc.aiaa.org | DOI: 10.2514/6.2017-0783

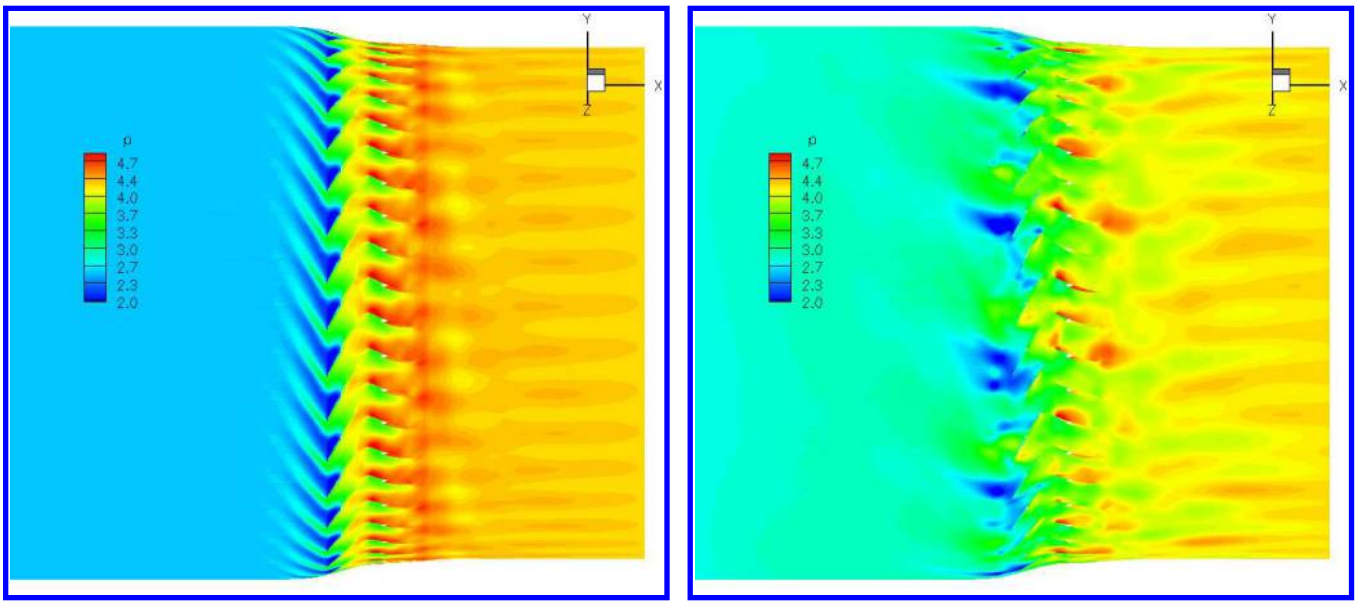

Figure 28: Pressure contours at the tip span before rotating stall. Left: URANS, Right: DDES

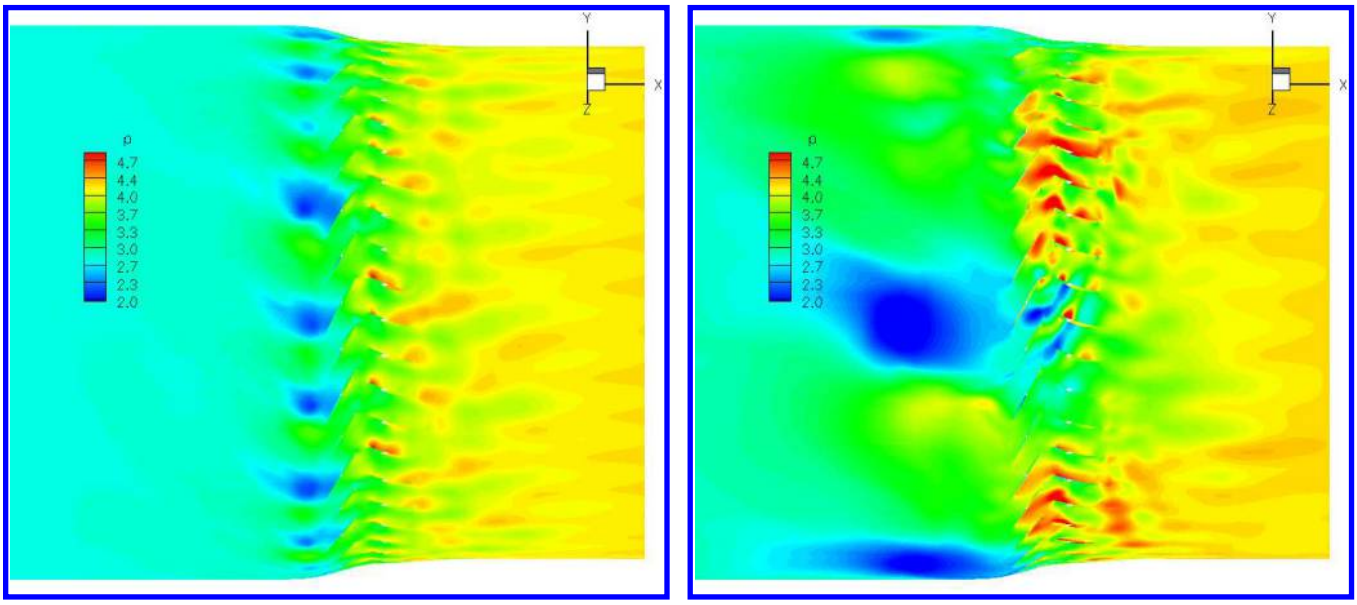

Figure 29: Pressure contours at the tip span at 4 revs rotating stall. Left: URANS, Right: DDES

Downloaded by Gecheng Zha on March 3, 2017 | http://arc.aiaa.org | DOI: 10.2514/6.2017-0783

Downloaded by Gecheng Zha on March 3, 2017 | http://arc.aiaa.org | DOI: 10.2514/6.2017-0783

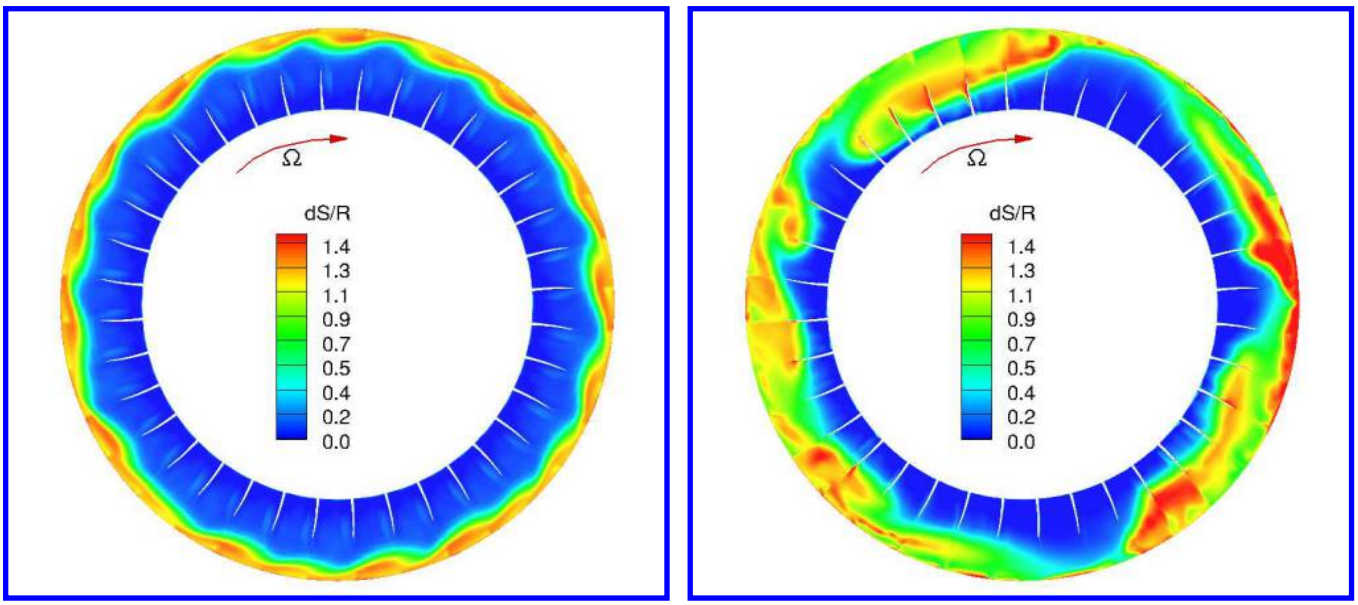

Figure 30: Entropy contours during rotating stall. Left: URANS, Right: DDES

7 Conclusions

A high fidelity methodology of 3-D fluid-structural interaction is presented for predicting blade flutter in a transonic compressor stage with rotor-stator interaction at near stall conditions. The full 3D unsteady Navier-Stokes equations are solved with Spalart Allmaras turbulence model. The flow solver and the structural solver are fully coupled via pseudo time step within each physical time step. An efficient and accurate modal approach solver is used for simulating the structural responses with the first five major mode shapes of the blade. The NASA Stage 35 is selected to demonstrate the methodology and simulation capability.

The steady state flow field computed on a single blade passage domain compare favorably with experimental data for NASA Stage 35. The rotor stall starts at point E and the fully developed rotated stall is captured.

The fully coupled FSI simulation is conducted along the speedline. For all the operating points, the amplitude of the blade vibration increase gradually and the blade appear to flutter without adding structural damping to the vibration system. With a structural damping coefficient of 0.001, the blade are damped before the stalling point E. However, the blade vibration response diverges at stalling point E with flutter.

The amplitude of blades vibration predicted by DDES is higher than that of URANS. The DDES method predict more small flow structures than the URANS method. The onset of rotating stall in the results of DDES starts earlier than that of URANS.

Downloaded by Gecheng Zha on March 3, 2017 | http://arc.aiaa.org | DOI: 10.2514/6.2017-0783

Acknowledgement

The simulation is conducted at the Center of Computational Sciences at the University of Miami.

References

[1] J. Lepicovsky, R. V. Chima, T. A. Jett, T. J. Bencic, and K. E. Weiland, "Investigation of flow separation in a transonic-fan linear cascade using visualization methods," *NASA/TM-2000-210521*, Dec 2000.

[2] Shaw, L.M., Boldman, D.R, and Buggele, A.E, "Unsteady Pressure Measurements on a Biconvex Airfoil in a Transonic Oscillating Cascade." NASA TM-86914, 1985.

[3] K. Isomura, and M.B. Giles, "A Numerical Study of Flutter in a Transonic Fan," *Journal of Turbomachinery*, vol. 120, pp. 500–507, 1998.

[4] P. Vasanthakumar, "Computation of Aerodynamic Damping for Flutter Analysis of a Transonic Fan." GT2011-46597, 2011.

[5] J.W. Chew, R.J. Hamby, J.G. Marshall, and M. Vahdati, " Part Speed Flutter of Transonic Fan." RTO AVT Symposium on Design Principles and Methods for Aircraft Gas Turbine Engines, Toulouse, France, May 1998, 1998.

[6] M. Vahdati, G. Simpson, and M. Imregun, "Mechanisms for Wide-Chord Fan Blade Flutter," *Journal of Turbomachinery*, vol. 133, pp. 041029–1–041029–7, 2011.

[7] R. Srivastava, and T.G. Keith Jr., "Influence of Shock Wave on Turbomachinery Blade Row Flutter," *Journal of Propulsion and Power*, vol. 21, pp. 167–174, 2005.

[8] H.-S. Im, and G.-C. Zha, "Flutter Prediction of a Transonic Fan with Traveling Wave Using Fully Coupled Fluid/Structure Interaction." ASME Paper GT2013-94341, Proceedings of ASME Turbo Expo, San Antonio, Texas, USA, 2013.

[9] R. Kamakoti, and W. Shyy, "Fluid-Structure Interaction for Aeroelastic Applications," *Progress in Aerospace Sciences*, vol. 40, pp. 535–558, 2004.

[10] V. Gnesin, and R. Rzadkowski, "A Coupled Fluid-Structure Analysis for 3-D Inviscid Flutter of IV Standard Configuration," *Journal of Sound and Vibration*, vol. 251, pp. 315–327, 2002.

[11] H. Doi, and J.J. Alonso, "Fluid/Structure Coupled Aeroelastic Computations for Transonic Flows in Turbomachinery." GT2002-30313,Proceedings of ASME Turbo Expo 2002, 2002.

[12] V. Carstens, R. Kemme, and S. Schmitt, "Coupled Simulation of Flow-Structrue Interaction in Turbomachinery," *Aerospace Science and Technology*, vol. 7, pp. 298–306, June 2003.

[13] A.I. Sayma, M.V. Vahdati, and M. Imregun, "Turbine Forced Response Prediction Using an Integrated Non-Linear Analysis," *Proceedings of the Institution of Mechanical Engineers, Part K: Journal of Multi-body Dynamics*, vol. 214, pp. 45–60, 2000.

[14] R. Srivastava, and T. S. R. Reddy, "Comparative Study of Coupled-Mode Flutter-Analysis Methods for Fan Configurations," *Journal of Propulsion and Power*, vol. 15, pp. 447–453, May-June 1999.

[15] X.Y. Chen, G.-C. Zha, M.-T. Yang, "Numerical Simulation of 3-D Wing Flutter with Fully Coupled Fluid-Structural Interaction," *Journal of Computers & Fluids*, vol. 36, pp. 856–867, 2007, doi:10.1016/j.compfluid.2006.08.005.

[16] H. Im, X. Chen, and G. Zha, "Prediction of a Supersonic Flutter Boundary Using a High Fidelity Delayed Detached Eddy Simulation." 50th AIAA Aerospace Sciences Meeting, Nashville, Tennessee, Jan. 2012, 2012.

Downloaded by Gecheng Zha on March 3, 2017 | http://arc.aiaa.org | DOI: 10.2514/6.2017-0783

[17] Gan, J.Y., Im, H.S., Chen, X.Y., Pasiliao, C.L. and Zha, G.C., "Prediction of Wing Flutter Boundary Using High Fidelity Delayed Detached Eddy Simulation." AIAA Paper 2015, Kissimmee, Florida, Jan. 2015.

[18] Zha, G.C., Shen, Y.Q., and Wang, B.Y., "Calculation of Transonic Flows Using WENO Method with a Low Diffusion E-CUSP Upwind Scheme." AIAA Paper 2008-0745, 46th AIAA Aerospace Sciences Meeting, Reno, NV, Jan. 2008.

[19] Y.Q. Shen, B.Y. Wang, and G.C. Zha, "Implicit WENO Scheme and High Order Viscous Formulas for Compressible Flows ." AIAA Paper 2007-4431, 2007.

[20] B. Wang, Z. Hu, and G. Zha, "A General Sub-Domain Boundary Mapping Procedure For Structured Grid CFD Parallel Computation," *AIAA Journal of Aerospace Computing, Information, and Communication*, vol. 5, pp. 425–447, 2008.

[21] P.R. Spalart, and S.R. Allmaras, "A One-equation Turbulence Model for Aerodynamic Flows." AIAA-92-0439, 1992.

[22] A. Jameson, "Time Dependent Calculations Using Multigrid with Applications to Unsteady Flows Past Airfoils and Wings." AIAA Paper 91-1596, 1991.

[23] A.J. Strazisar, J.R. Wood, M.D. Hathaway, and K.L. Suder, "Laser Anemometer Measurements in a Transonic Axial-Flow Fan Rotor." NASA Technical Paper 2879, November, 1989.

[24] Y. Gong, "A Computational Model for Rotating Stall and Inlet Distortions in Multistage Compressors." Ph.D. Thesis, Massachusetts Institute of Technology, Feb. 1999.

[25] M. Inoue, M. Kuroumaru, T. Tanino, S. Yoshida, and M. Furukawa, "Comparative Studies on Short and Long Length-Scale Stall Cell Propagating in an Axial Compressor Rotor," *AMSE J. of Turbomach.*, vol. 123, pp. 24–31, 2001.

[26] D.A. Hoying, C.S. Tan, H.D. Vo, and E.M. Greitzer, "Role of Blade Passage Flow Structures in Axial Compressor Rotating Stall Inception," *AMSE J. of Turbomach.*, vol. 121, pp. 735–742, doi:10.1115/1.2836727, 1999.

[27] H.S. Im, X.Y. Chen, and G.C. Zha, "Simulation of 3D Multistage Axial Compressor Using a Fully Conservative Sliding Boundary Condition." ASME IMECE2011-62049, International Mechanical Engineering Congress & Exposition, Denver, November 2011, 2011.

[28] L. Reid, and R.D. Moore, "Design and Overall Performance of Four Highly-Loaded, High Speed Inlet Stages for an Advanced, High Pressure Ratio Core Compressor." NASA TP.1337, 1978.

[29] Gan, J.Y., Im, H.S., and Zha, G.C., "Simulation of stall inception of a high speed axial compressor with rotor-stator interaction." 51st AIAA/SAE/ASEE Joint Propulsion Conference, Orlando, FL, July. 2015.

Downloaded by Gecheng Zha on March 3, 2017 | http://arc.aiaa.org | DOI: 10.2514/6.2017-0783